

IRTF: A new tensor factorization for irregular multidimensional data recovery

Jin-Yu Xie ^a, Hao Zhang ^{b,*}, Xi-Le Zhao ^a, Yi-Si Luo ^c

^a School of Mathematical Sciences, University of Electronic Science and Technology of China, Chengdu, Sichuan Province, 611731, China

^b School of Computing and Artificial Intelligence, Southwest Jiaotong University, Chengdu, Sichuan Province, 611756, China

^c School of Mathematics and Statistics, Xi'an Jiaotong University, Xi'an, Shaanxi Province, 710049, China

ARTICLE INFO

Keywords:

Tensor factorization
Irregular multidimensional data
Total variation

ABSTRACT

Tensor factorizations, although serving as paramount tools for exploiting prior knowledge of multidimensional data, are unsuitable for emerging irregular multidimensional data with the arbitrary shape spatial domain (i.e., spatial-irregular tensor), such as superpixels and spatial transcriptomics. Developing new tensor factorizations suitable for spatial-irregular tensors poses a compelling challenge. To meet this challenge, we introduce a novel Irregular Tensor Factorization (IRTF), which can fully capture the intrinsic spatial and channel information behind the spatial-irregular tensor. Concretely, a spatial-irregular tensor can be decomposed into the product of an intrinsic regular tensor, learnable channel transform matrices, and a learnable spatial transform matrix. Accompanying IRTF, we suggest the Total Variation on Channel and Spatial Transforms (TV-CST) to exploit the local information of spatial-irregular tensors, which is hardly excavated by traditional total variation methods. Combining the proposed IRTF and TV-CST, we built a spatial-irregular tensor recovery model. Extensive experiments on real-world spatial-irregular tensors demonstrate the promising performance of our IRTF and its significant advantages on downstream tasks.

1. Introduction

With the rapid advancement of data science, the prevalence of multidimensional data with multiple dimensions has significantly increased. However, such data often encounters disturbances, such as elements missing [1] and noise [2], which hinder its applications in various domains, such as object detection [3], image segmentation [4], and image classification [5,6]. Consequently, data recovery techniques are required to enhance the quality of these observed data for subsequent tasks.

Real-world multidimensional data can be mathematically represented by the tensor [7,8]. In this paper, we specifically focus on third-order tensors. Classical third-order tensors can be conceptualized as collections of equally-sized rectangular slices (i.e., the regular tensor), such as RGB images, multispectral images (MSI), hyperspectral images (HSI), and grayscale videos. These third-order tensors possess two spatial dimensions and one spectral or temporal dimension.

Tensor factorizations are powerful and fundamental tools for leveraging the correlations among different modes of the tensor. They decompose a tensor into a series of compact matrix/tensor factors with a

specific interaction. Existing tensor factorization methods for the regular tensor mainly include CANDECOMP/PARAFAC (CP) factorization [9,10], Tucker factorization [11,12], tensor singular value decomposition [13–15], and tensor network factorizations [16–18]. These methods can also be called traditional tensor factorizations. Traditional tensor factorizations-based methods achieve significant success in multidimensional data recovery.

Spatial-irregular multidimensional data: Recently, spatial-irregular multidimensional data has been emerging, such as semantic units from image segmentation algorithms (e.g., segment anything model [19] and superpixels segmentation algorithms [20,21]) and spatial transcriptomics data from bioinformatics [22]. Fig. 1 provides two real-world examples of the spatial-irregular multidimensional data. The spatial-irregular multidimensional data is a tensor (i.e., spatial-irregular tensor), whose spatial domain is an arbitrary shape and tubes are the same length.

Limitations of existing methods: Traditional tensor factorizations are designed for the regular tensor, whose frontal slices are rectangles of the same size (see Fig. 2 (a)). Thus, traditional tensor factorizations cannot be directly applied to irregular tensors. Recently, PARAFAC2

* Corresponding author.

E-mail addresses: xiejinyu554@gmail.com (J.-Y. Xie), aaronzhangfy@163.com (H. Zhang), xlzhao122003@163.com (X.-L. Zhao), yisiluo1221@foxmail.com (Y.-S. Luo).

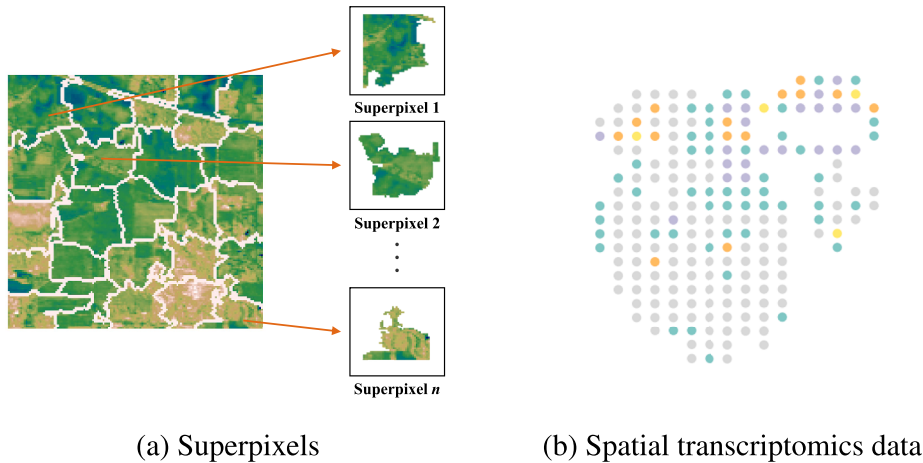


Fig. 1. Real-world examples of the spatial-irregular multidimensional data. (a) The semantic units (i.e., superpixels) from HSI *Indian Pines* by superpixels segmentation algorithms. (b) Spatial transcriptomics data of the human heart visualized in 2D.

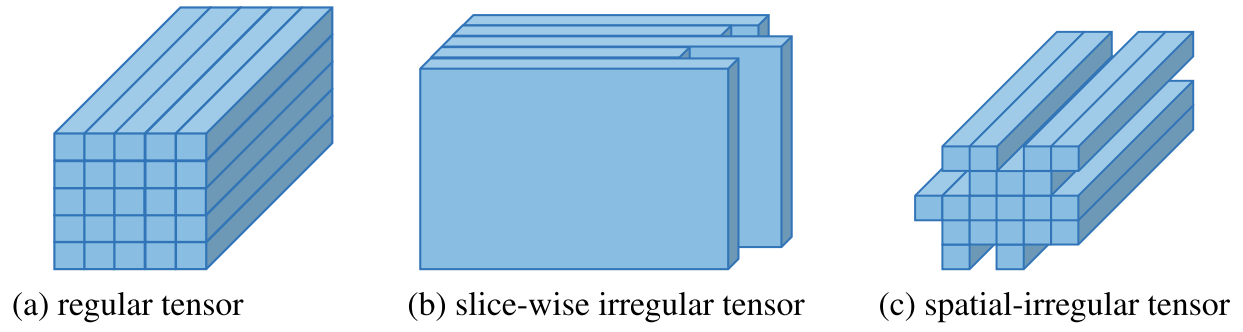


Fig. 2. Examples of different types of tensors.

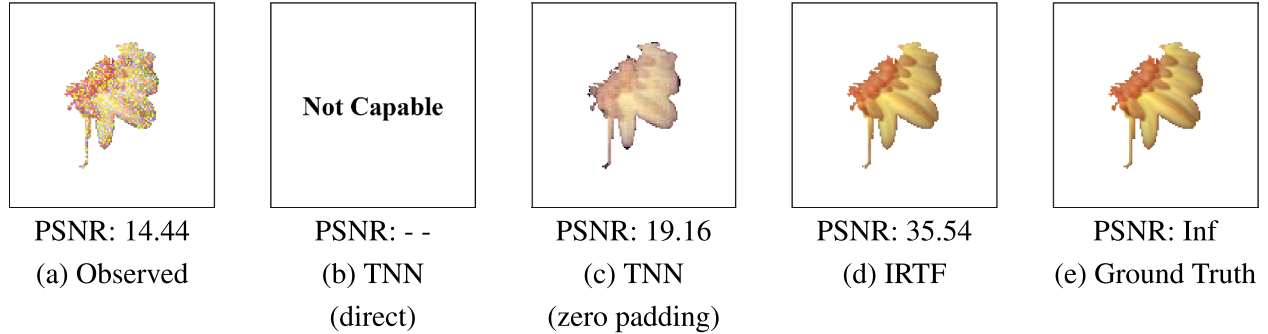


Fig. 3. An experimental example of spatial-irregular tensor denoising. Here, the spatial-irregular tensor is a superpixel from MSI *flowers*.

factorization has been introduced for the slice-wise irregular tensor, whose frontal slices are rectangles of different sizes (see Fig. 2 (b)). However, the frontal slices of the spatial-irregular tensor are an arbitrary shape (see Fig. 2 (c)), which is more challenging. PARAFAC2 factorization is not suitable for the more complex spatial-irregular tensor.

By using preprocessing (e.g., zero padding), we can transform the spatial-irregular tensor into a regular tensor, and then apply traditional tensor factorization-based methods (e.g., tensor nuclear norm (TNN)) to the resulting regular tensor. However, the preprocessing inevitably introduces extra errors, leading to artifacts (see Fig. 3 (c)). In summary, existing methods suffer significant limitations for the emerging spatial-irregular multidimensional data. This situation summons the development of a novel tensor factorization for representing the emerging spatial-irregular multidimensional data, which can allow us to exploit information of spatial-irregular multidimensional data.

In response, we propose a new tensor factorization to represent the spatial-irregular multidimensional data (termed as IRTF), which can fully capture the intrinsic spatial and channel information behind the spatial-irregular tensor. Specifically, IRTF represents the irregular tensor by an intrinsic regular tensor multiplied by a learnable channel transform and a learnable spatial transform. Here, the intrinsic regular tensor reveals the intrinsic information of the original irregular tensor. The spatial transform not only transforms the spatial-irregular tensor into a regular tensor but also preserves the intrinsic spatial information of the original data. The channel transform is a hierarchical nonlinear transform, which fully exploits the complex nonlinear structure within channels. Based on the proposed IRTF, to further exploit the local smoothness of the recovered spatial-irregular multidimensional data, we suggest a total variation (TV) on channel and spatial transforms (termed as TV-CST), where the standard TV cannot be directly deployed to the original

irregular tensor. By integrating the proposed IRTF and TV-CST, we establish an irregular multidimensional data recovery model. From Fig. 3 (d), we can observe that our method preserves the color and the edge of the spatial-irregular multidimensional data as compared with traditional tensor factorization with preprocessing.

In summary, the contributions of this paper can be summarized as follows:

(i) To meet the challenge of spatial-irregular multidimensional data representation, we introduce a novel tensor factorization specifically designed for spatial-irregular tensors (i.e., the IRTF), which naturally reveals the essential information of the spatial-irregular multidimensional data.

(ii) To exploit the local smoothness of the spatial-irregular tensor, we introduce the TV on channel and spatial transforms (termed as TV-CST) based on the proposed IRTF, where standard TV cannot be directly deployed to the original spatial-irregular tensor. Then, we establish the connection between TV-CST and the standard TV.

(iii) Empowered with IRTF and TV-CST, we develop the corresponding irregular multidimensional data recovery model. Extensive experiments demonstrate the superior performance of our method compared to existing methods on spatial-irregular tensor recovery and subsequent clustering and classification tasks.

2. Related work

Here, we introduce existing tensor factorization-based methods for regular tensor recovery and irregular tensor recovery in detail.

Regular tensor recovery methods: Tensor factorization-based methods for regular tensor recovery are mainly based on CP factorization, Tucker factorization, tensor singular value decomposition, and tensor network factorization. CP factorization [9,10] decomposes a tensor as the sum of the rank-one tensors. Zhao et al. [23] designed a Bayesian CP factorization for image recovery. Tucker factorization [11,12] decomposes a tensor into a core tensor multiplied by matrices along each mode. Liu et al. [24] proposed a Tucker factorization-based low-rank metric (i.e., the sum of the nuclear norm) and applied it to image recovery. Xu et al. [25] introduced parallel matrix factorization to accelerate the Tucker factorization-based low-rank approximation. Tensor network factorizations, like tensor train (TT) factorization [17] and tensor ring (TR) factorization [18,26], were developed to effectively capture the low-rank structure of multidimensional data with dimensions more than three. For the third-order tensor recovery, it usually needs to use tensor augmentation to convert the third-order tensor to a higher-order tensor and then apply the tensor network factorization [27–29]. Based on the new tensor-tensor product (t-product), tensor singular value decomposition (t-SVD) decomposes a tensor into t-products of two orthogonal tensors and a f-diagonal tensor [30]. T-SVD introduced a low-rank metric (i.e., TNN) [13,31]. Many multidimensional data recovery methods were developed based on the TNN framework [14,32–34]. However, these traditional tensor factorizations cannot be directly applied to irregular tensors.

Irregular tensor recovery methods: Recently, PARAFAC2 factorization is introduced to handle the slice-wise irregular tensor, whose frontal slices are rectangles of different sizes. PARAFAC2 factorization can apply the same factor along one mode and allows the other factor matrices to vary in the mode, thus being suitable for slice-wise irregular tensor [35–39]. Afshar et al. [40] proposed a constrained PARAFAC2 factorization, which incorporates temporal smoothness, sparsity, and non-negativity in the resulting factors. Ren et al. [41] proposed a robust PARAFAC2 factorization, which can handle erroneousness and missing data. Jang et al. [42] designed a fast and scalable PARAFAC2 factorization, which is efficient while achieving comparable accuracy. Different from the slice-wise irregular tensor, the frontal slices of the spatial-irregular tensor are an arbitrary shape, which is more challenging. PARAFAC2 factorization-based methods cannot handle the more complex spatial-irregular tensor.

Table 1
Notations used in this paper.

Notations	Explanation
$x, \mathbf{x}, \mathbf{X}, \mathcal{X}$	scalar, vector, matrix, tensor
$\mathcal{X}(i, j, k)$	the (i, j, k) -th element of the third-order tensor \mathcal{X}
$\mathcal{X}(:, :, i)$, $\mathcal{X}(i)$	the i -th slice of the third-order tensor \mathcal{X}
$\ \mathcal{X}\ _F$	the Frobenius norm: $\ \mathcal{X}\ _F = \sqrt{\sum_{ijk} \mathcal{X}(i, j, k)^2}$
$\ \mathcal{X}\ _{\ell_1}$	the ℓ_1 -norm: $\ \mathcal{X}\ _{\ell_1} = \sum_{ijk} \mathcal{X}(i, j, k) $
$\sigma_i(\mathbf{X})$	the i -th singular value of \mathbf{X}
\mathbb{Z}_+	the set of the positive integers
$\mathbf{A} \otimes \mathbf{B}$	the Kronecker product of matrices \mathbf{A} and \mathbf{B}

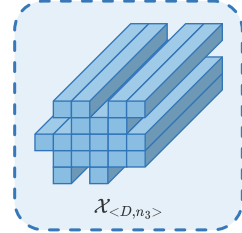


Fig. 4. An example of the spatial-irregular tensor.

In summary, existing methods are not suitable for the emerging spatial-irregular multidimensional data while our method is a promising alternative.

3. Notations and preliminaries

Some common symbols used in this paper are provided in Table 1. The unfolding operator of a regular tensor $\mathcal{X} \in \mathbb{R}^{n_1 \times n_2 \times n_3}$ along the i -th mode ($i = 1, 2, 3$) is defined as $\text{unfold}_i(\cdot) : \mathbb{R}^{n_1 \times n_2 \times n_3} \rightarrow \mathbb{R}^{n_i \times \prod_{j \neq i} n_j}$. And $\text{fold}_i(\cdot)$ denotes the inverse operator of $\text{unfold}_i(\cdot)$. $\text{unfold}_i(\mathcal{X})$ is denoted as $\mathbf{X}_{(i)}$. Additionally, the mode- i product between \mathcal{X} and \mathbf{A} is defined as $\mathcal{X} \times_i \mathbf{A} \triangleq \text{fold}_i(\mathbf{A} \text{unfold}_i(\mathcal{X})) = \text{fold}_i(\mathbf{A} \mathbf{X}_{(i)})$ [35].

4. The proposed method

In this section, we first provide the basic definition and some operations for the spatial-irregular tensor and then introduce the proposed method based on these definitions and operations.

4.1. Basic definitions and operators for irregular tensor

Since basic definitions and operators for spatial-irregular tensors are lacking, we develop the corresponding definitions and operators for spatial-irregular tensors.

Definition 1 (Spatial-Irregular Tensor). Give an index set $\mathbb{Z}_+^2 \triangleq \{(i, j) | i \in \mathbb{Z}_+, j \in \mathbb{Z}_+\}$ and an index set $D \subseteq \mathbb{Z}_+^2$, where D is a non-rectangle domain. If the index (i, j, k) of elements of a tensor \mathcal{X} satisfies $(i, j) \in D$ and $1 \leq k \leq n_3$, \mathcal{X} is a spatial-irregular tensor, denoted as $\mathcal{X}_{<D,n_3>}$, whose spatial index belong to D and tubes have the same length n_3 .

Fig. 4 provides an example of the spatial-irregular tensor.

With the definition of the spatial-irregular tensor, we can define the unfolding and folding operators for the spatial-irregular tensor.

Definition 2 (Unfolding for Spatial-Irregular Tensor). For a spatial-irregular tensor $\mathcal{X}_{<D,n_3>}$, $|D|$ is denoted as the cardinality of the spatial domain D . Then, the unfolding for the spatial-irregular tensor is

$$\hat{\mathbf{X}}_{<D,n_3>} = \text{ir-unfold}(\mathcal{X}_{<D,n_3>}, D) \triangleq [\mathcal{X}_{<D,n_3>_{(1)}}, \dots, \mathcal{X}_{<D,n_3>_{(|D|)}}], \quad (1)$$

where $\hat{\mathbf{X}}_{<D,n_3>} \in \mathbb{R}^{n_3 \times |D|}$ and $\mathcal{X}_{<D,n_3>_{(q)}} \in \mathbb{R}^{n_3}$ is the q -th tube of $\mathcal{X}_{<D,n_3>}$ ($q = 1, 2, \dots, |D|$).

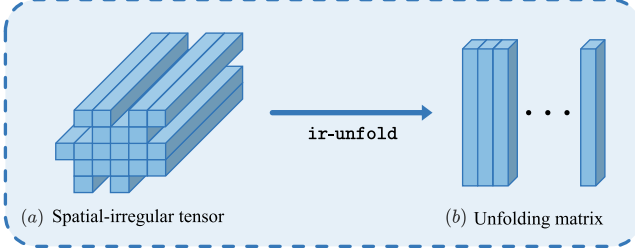


Fig. 5. An example of the unfolding for a spatial-irregular tensor.

As the tubes of the spatial-irregular tensor are the same length (see Fig. 5 (a)), the ir-unfold operator arranges these same-length tubes into a matrix (see Fig. 5 (b)). The inverse operator of ir-unfold is the folding operator, defined as $\mathcal{X}_{\langle D, n_3 \rangle} = \text{ir-fold}(\hat{\mathbf{X}}_{\langle D, n_3 \rangle}, D)$, where D denotes the irregular index set.

Based on the unfolding and folding operators, we define the following irregular tensor-matrix product.

Definition 3 (Irregular Tensor-Matrix Product). Given a spatial-irregular tensor $\mathcal{X}_{\langle D_1, n_3 \rangle}$, spatial index set D_2 , and a matrix $\mathbf{A} \in \mathbb{R}^{|D_1| \times |D_2|}$, the product of $\mathcal{X}_{\langle D_1, n_3 \rangle}$ and \mathbf{A} is defined as:

$$\mathcal{Y}_{\langle D_2, n_3 \rangle} = \mathcal{X}_{\langle D_1, n_3 \rangle} \times_{D_2} \mathbf{A} \triangleq \text{ir-fold}(\text{ir-unfold}(\mathcal{X}_{\langle D_1, n_3 \rangle}, D_1) \mathbf{A}, D_2). \quad (2)$$

Fig. 6 provides an example of the irregular tensor-matrix product.

4.2. The proposed IRTF

Based on the previous definitions, we can formally introduce the proposed IRTF, which allows us to fully exploit the local smoothness and

low-rankness of the spatial-irregular tensor as compared with traditional tensor factorizations. Fig. 7 provides a flowchart of the proposed IRTF. Here, a spatial-irregular tensor is represented by the product of an intrinsic regular tensor, a learnable channel transform, and a learnable spatial transform. Then, the intrinsic local smoothness and low-rankness behind the spatial-irregular tensor can be exploited by the smoothness regularizer on the spatial and channel transforms matrices and low-rankness regularizer on the latent regular tensor, respectively.

Next, we introduce IRTF with the learnable channel and learnable spatial transforms, regularization on factors of IRTF, and IRTF-based spatial-irregular tensor recovery model in detail.

Definition 4 (IRTf). Given an irregular tensor $\mathcal{X}_{\langle D, n_3 \rangle}$, we define its parametric representation form (called the IRTF of $\mathcal{X}_{\langle D, n_3 \rangle}$) by using the learnable channel transform $g_{\mathbf{H}}(\cdot)$ with parameter matrices $\mathbf{H} \triangleq \{\{\mathbf{H}_i\}_{i=1}^K\}$, the learnable spatial transform $h_{\mathbf{W}}(\cdot)$ with a parameter matrix $\mathbf{W} \in \mathbb{R}^{m_1 m_2 \times |D|}$, and the learnable intrinsic tensor $\mathcal{Z} \in \mathbb{R}^{m_1 \times m_2 \times m_3}$, i.e.,

$$\mathcal{X}_{\langle D, n_3 \rangle} = h_{\mathbf{W}}(g_{\mathbf{H}}(\mathcal{Z})). \quad (3)$$

In IRTF, start with \mathcal{Z} , which preserves the intrinsic information of the original spatial-irregular; Then, with the help of the learnable channel transform, $g_{\mathbf{H}}(\mathcal{Z})$ exploits the nonlinear characteristic along the third mode; Next, by the learnable spatial transform, $h_{\mathbf{W}}(\cdot)$ bridges $g_{\mathbf{H}}(\mathcal{Z})$ and the original spatial-irregular multidimensional data.

Now, we introduce the structures of channel and spatial transforms in detail.

Learnable channel transform: The learnable channel transform is to exploit the internal nonlinear characteristic of the spatial-irregular data. To capture the nonlinear characteristic, we introduce a hierarchical nonlinear transform $g_{\mathbf{H}}(\mathcal{Z})$ conditioned on the latent tensor $\mathcal{Z} \in \mathbb{R}^{m_1 \times m_2 \times m_3}$, which aims to characterize the hierarchical nonlinear

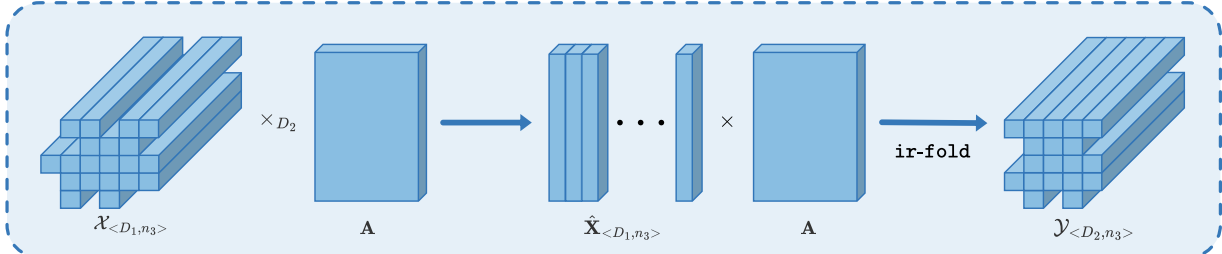


Fig. 6. An example of irregular tensor-matrix product.

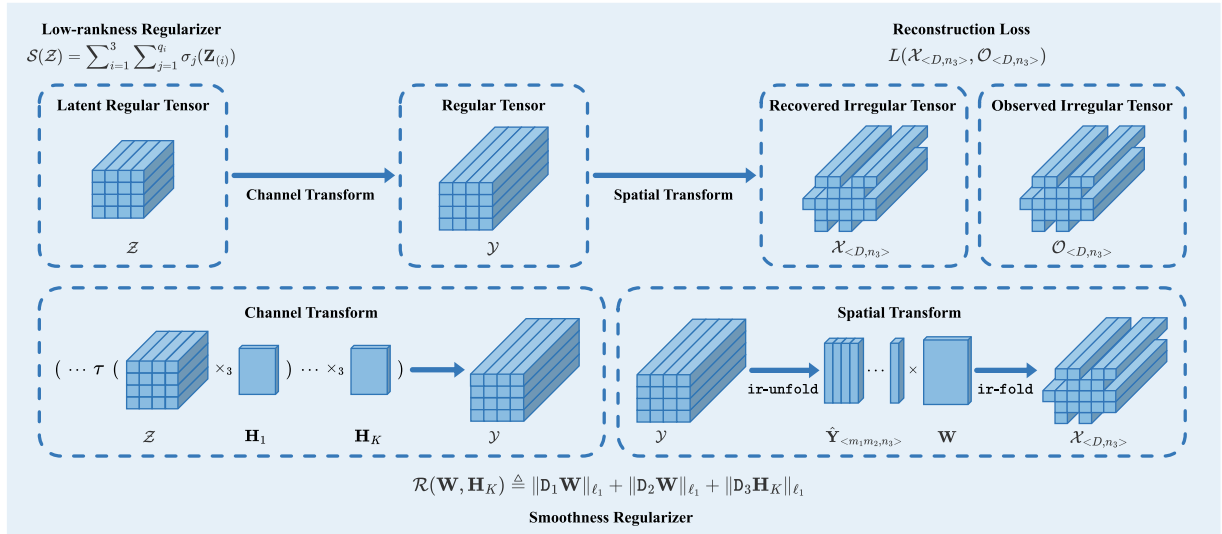


Fig. 7. The flowchart of the proposed IRTF method on spatial-irregular data recovery task.

structures of \mathcal{Y} by parameterizing it through:

$$\mathcal{Y} = g_{\mathbf{H}}(\mathcal{Z}) = \tau(\cdots \tau(\mathcal{Z} \times_3 \mathbf{H}_1) \times_3 \mathbf{H}_2 \cdots) \times_3 \mathbf{H}_K. \quad (4)$$

Here $\mathbf{H} \triangleq \{\mathbf{H}_i \in \mathbb{R}^{m_3 \times m_3}\}_{i=1}^{K-1}$, $\mathbf{H}_K \in \mathbb{R}^{n_3 \times m_3}$ are learnable channel transform matrices, K is the number of layers in the nonlinear transform, and $\tau(\cdot)$ denotes the nonlinear activation function.

Learnable spatial transform: The learnable spatial transform aims to bridge the resulting regular tensor $g_{\mathbf{H}}(\mathcal{Z})$ and the original irregular tensor. For a given spatial-irregular tensor $\mathcal{X}_{\langle D, n_3 \rangle}$, we define the learnable spatial transform $h_{\mathbf{W}}(\cdot)$ with a parameter matrix $\mathbf{W} \in \mathbb{R}^{m_1 m_2 \times |D|}$ and then use the following parameterization form to represent the irregular tensor $\mathcal{X}_{\langle D, n_3 \rangle}$:

$$\mathcal{X}_{\langle D, n_3 \rangle} = h_{\mathbf{W}}(\mathcal{Y}) = \mathcal{Y} \times_D \mathbf{W}, \quad (5)$$

where $\mathcal{Y} \in \mathbb{R}^{m_1 \times m_2 \times n_3}$ is the resulting regular tensor obtained by the learnable channel transform, i.e., $g_{\mathbf{H}}(\mathcal{Z})$. The spatial transform $h_{\mathbf{W}}(\cdot)$ enables us to characterize the intrinsic structures of the irregular tensor $\mathcal{X}_{\langle D, n_3 \rangle}$ by substitutively characterizing it on a spatial regular tensor, i.e., the tensor \mathcal{Y} , followed by the spatial transform $h_{\mathbf{W}}(\cdot)$ to convert \mathcal{Y} to the original irregular tensor. Here, the parameter \mathbf{W} can be a discrete Fourier transform (DFT), discrete cosine transform (DCT), or even a learnable matrix. In this work, we consider setting \mathbf{W} as a learnable matrix, which encodes more flexibility to represent the irregular data.

4.3. Regularization on factors of IRTF

Due to the non-rectangular spatial domain, exploiting inherent prior information (e.g., local smoothness and low-rankness) of the spatial-irregular data is difficult by traditional methods, e.g., standard TV regularization and traditional low-rank tensor regularizations on the original data. The proposed IRTF allows us to address this problem. Under the parameterized IRTF, we can further exploit the local smoothness and low-rankness of the spatial-irregular tensor by performing regularizations on factors of IRTF. Here, we will provide a detailed introduction to exploit the local smoothness and low-rankness of the spatial-irregular tensor by regularization on factors from IRTF and establish the connection with regularization on factors and corresponding regularization on the original data.

Local Smoothness: Traditional TV has been widely used to promote local smoothness in tensors. However, its application to irregular tensors has not been explored extensively. The proposed IRTF provides us with an opportunity to address this gap. In this paper, we present a novel TV on the channel and spatial transforms matrices (termed as TV-CST), which is specifically designed to exploit both channel and spatial smoothness in irregular tensors. Mathematically, the TV-CST regularization term is formulated as follows

$$\mathcal{R}(\mathbf{W}, \mathbf{H}_K) \triangleq \|\mathbf{D}_1 \mathbf{W}\|_{\ell_1} + \|\mathbf{D}_2 \mathbf{W}\|_{\ell_1} + \|\mathbf{D}_3 \mathbf{H}_K\|_{\ell_1}. \quad (6)$$

Here $\|\mathbf{D}_1 \mathbf{W}\|_{\ell_1} \triangleq \sum_{(i,j),(i+1,j) \in D} \sum_{k=1}^{m_1 m_2} |\mathcal{W}(i+1, j, k) - \mathcal{W}(i, j, k)|$, $\|\mathbf{D}_2 \mathbf{W}\|_{\ell_1} \triangleq \sum_{(i,j),(i,j+1) \in D} \sum_{k=1}^{m_1 m_2} |\mathcal{W}(i, j+1, k) - \mathcal{W}(i, j, k)|$, where $\mathcal{W} = \mathcal{W}_{\langle D, m_1 m_2 \rangle} = \text{ir-fold}(\mathbf{W}, D)$ for simplicity. $\|\mathbf{D}_3 \mathbf{H}_K\|_{\ell_1} \triangleq \|\mathbf{H}_K(2:n_3, :) - \mathbf{H}_K(1:n_3-1, :)\|_{\ell_1}$.

Next, we discuss the connections between TV-CST regularization and the traditional 3DTV regularization [43], which support the effectiveness of our proposed TV-CST.

Theorem 1. Suppose that the spatial index set D is regular and $\mathcal{X} = h_{\mathbf{W}}(g_{\mathbf{H}}(\mathcal{Z})) \in \mathbb{R}^{n_1 \times n_2 \times n_3}$. Assume that the ℓ_1 -norm of \mathcal{Z}, \mathbf{W} , and $\{\mathbf{H}_j\}_{j=1}^K$ is bounded by η , and $\tau(\cdot)$ is Lipschitz continuous with Lipschitz constant κ . Then the following inequalities hold:

$$\|\mathbf{D}_x \mathcal{X}\|_{\ell_1} \leq \kappa^{K-1} \eta^{K+1} \|\mathbf{D}_1 \mathbf{W}\|_{\ell_1}, \quad (7a)$$

$$\|\mathbf{D}_y \mathcal{X}\|_{\ell_1} \leq \kappa^{K-1} \eta^{K+1} \|\mathbf{D}_2 \mathbf{W}\|_{\ell_1}, \quad (7b)$$

$$\|\mathbf{D}_z \mathcal{X}\|_{\ell_1} \leq \kappa^{K-1} \eta^{K+1} \|\mathbf{D}_3 \mathbf{H}_K\|_{\ell_1}, \quad (7c)$$

where $\|\mathbf{D}_x \mathcal{X}\|_{\ell_1} \triangleq \|\mathcal{X}(2:n_1, :, :) - \mathcal{X}(1:n_1-1, :, :)\|_{\ell_1}$. The definitions of $\|\mathbf{D}_y \mathcal{X}\|_{\ell_1}$ and $\|\mathbf{D}_z \mathcal{X}\|_{\ell_1}$ are similar to $\|\mathbf{D}_x \mathcal{X}\|_{\ell_1}$.

Then, it holds that

$$\|\mathcal{X}\|_{3DTV} \triangleq \|\mathbf{D}_x \mathcal{X}\|_{\ell_1} + \|\mathbf{D}_y \mathcal{X}\|_{\ell_1} + \|\mathbf{D}_z \mathcal{X}\|_{\ell_1} \leq \kappa^{K-1} \eta^{K+1} \mathcal{R}(\mathbf{W}, \mathbf{H}_K). \quad (8)$$

Theorem 1 indicates that the traditional 3DTV regularization [43] is upper bounded by the proposed TV-CST. The results reveal that TV-CST exploits the local smoothness of $\mathcal{X}_{\langle D, n_3 \rangle}$. Specifically, the Eqs. (7a) and (7b) reveal that $\|\mathbf{D}_1 \mathbf{W}\|_{\ell_1}$ and $\|\mathbf{D}_2 \mathbf{W}\|_{\ell_1}$ can capture the spatial local smoothness, and the Eq. (7c) suggests that the regularization on the last layer of the channel transform, i.e., $\|\mathbf{D}_3 \mathbf{H}_K\|_{\ell_1}$, can exploit the channel local smoothness. The results reveal that TV-CST exploits the local smoothness of $\mathcal{X}_{\langle D, n_3 \rangle}$ along different modes. The proof is reported in supplementary material Appendix A.1.

Low-Rankness: To exploit the low-rankness of irregular tensors, we introduce the sum of the nuclear norm (SNN) [24] on the intrinsic regular tensor $\mathcal{Z} \in \mathbb{R}^{m_1 \times m_2 \times m_3}$, i.e.,

$$S(\mathcal{Z}) \triangleq \sum_{i=1}^3 \sum_{j=1}^{q_i} \sigma_j(\mathbf{Z}_{(i)}), \quad (9)$$

where $q_i = \min(m_i, \prod_{l \neq i} m_l)$.

Next, we discuss the connection between the SNN of the intrinsic regular tensor \mathcal{Z} and that of the original $\mathcal{X}_{\langle D, n_3 \rangle}$.

Theorem 2. Suppose that the index set D is regular and the channel transform is a linear transformation, i.e., $K = 1$. When $\mathbf{H}_1 \mathbf{H}_1^\top = \mathbf{I}$ and \mathbf{W} can be decomposed in Kronecker form, i.e., $\mathbf{W} = \mathbf{A} \otimes \mathbf{B}$, satisfying $\mathbf{A}^\top \mathbf{A} = \mathbf{I}$ ($\mathbf{A} \in \mathbb{R}^{m_2 \times n_2}$) and $\mathbf{B}^\top \mathbf{B} = \mathbf{I}$ ($\mathbf{B} \in \mathbb{R}^{m_1 \times n_1}$), then the following inequality holds:

$$S(\mathcal{X}) \leq S(\mathcal{Z}). \quad (10)$$

Theorem 2 states that the SNN of \mathcal{Z} is greater than that of \mathcal{X} , which indicates that when \mathcal{Z} is low-rank, \mathcal{X} is also low-rank. Hence, we can promote the low-rankness of \mathcal{X} by promoting the low-rankness of \mathcal{Z} , i.e., minimizing the SNN of \mathcal{Z} . The proof is reported in supplementary material Appendix A.2.

4.4. Irregular data recovery model

Equipped with the meticulously designed IRTF and TV-CST, we suggest a model for irregular data recovery, formulated as:

$$\min_{\mathbf{W}, \mathcal{Z}, \mathbf{H}} L(h_{\mathbf{W}}(g_{\mathbf{H}}(\mathcal{Z})), \mathcal{O}_{\langle D, n_3 \rangle}) + \lambda_1 \mathcal{R}(\mathbf{W}, \mathbf{H}_K) + \lambda_2 S(\mathcal{Z}), \quad (11)$$

where $\mathcal{O}_{\langle D, n_3 \rangle}$ is the observation, $\mathcal{Z} \in \mathbb{R}^{m_1 \times m_2 \times m_3}$ is the learnable intrinsic tensor, $g_{\mathbf{H}}(\cdot)$ is the channel transform with parameters $\mathbf{H} \triangleq \{\mathbf{H}_j\}_{j=1}^K$, $h_{\mathbf{W}}(\cdot)$ denotes the spatial transform with a learnable parameter matrix \mathbf{W} , and $\{\lambda_i\}_{i=1}^2$ are the trade-off parameters. L denotes the fidelity item. Note that the proposed model is unsupervised and only requires observations without any training dataset.

To evaluate the performance of our proposed model, we consider two representative data recovery tasks:

- **Irregular data denoising** aims at recovering a clean tensor from its noisy observation. We consider Gaussian noise and impulse noise. The fidelity item could be simply setting as $L(\mathcal{X}_{\langle D, n_3 \rangle}, \mathcal{O}_{\langle D, n_3 \rangle}) = \|\mathcal{X}_{\langle D, n_3 \rangle} - \mathcal{O}_{\langle D, n_3 \rangle}\|_{\ell_1}$, which can characterize the noise.
- **Irregular data completion** aims at recovering an underlying low-rank tensor from its incomplete observation. The fidelity item is $L(\mathcal{X}_{\langle D, n_3 \rangle}, \mathcal{O}_{\langle D, n_3 \rangle}) = \|(\mathcal{X}_{\langle D, n_3 \rangle} - \mathcal{O}_{\langle D, n_3 \rangle})_\Omega\|_F^2$, where the Ω is the support of observed entries.

To solve the highly non-convex problem Eq. (11), we use the efficient adaptive moment estimation algorithm (Adam) [44] to update the parameters $\Theta \triangleq \{\mathcal{Z}, \mathbf{W}, \{\mathbf{H}_j\}_{j=1}^K\}$.

Computational complexity: The forward computational complexity primarily comes from the channel transform, the spatial transform, and SNN. Specifically, given an irregular observation $\mathcal{X}_{\langle D, n_3 \rangle}$, the size of the core tensor \mathcal{Z} is set to $m_1 \times m_2 \times m_3$. The computational complexities of the channel and spatial transforms are $O(((K -$

Table 2

The average numerical results of superpixel denoising by different methods. The **best** and **second-best** values are highlighted. Note that all the compared traditional methods work on superpixels with zero padding.

Method		LRMR	LRTV	LRTDTV	E3DTV	HLRT F	LRCID	IRTF
Data	Case	PSNR(dB)/SSIM						
	Case 1	28.34/0.893	31.43/0.963	30.91/0.944	<u>32.99/0.969</u>	29.74/0.933	30.69/0.929	33.40/0.974
	Case 2	27.68/0.880	27.49/0.930	31.60/0.960	<u>32.09/0.963</u>	29.51/0.932	26.67/0.891	32.12/0.971
	Case 1	25.15/0.871	26.97/0.906	26.14/0.883	29.27/0.946	28.20/0.938	<u>29.38/0.947</u>	29.46/0.951
	Case 2	24.31/0.856	24.57/0.871	26.49/0.901	<u>28.57/0.942</u>	27.35/0.932	28.27/0.940	28.66/0.945
	Case 1	29.31/0.933	31.43/0.961	31.00/0.954	<u>31.88/0.967</u>	29.94/0.949	30.51/0.938	32.38/0.968
	Case 2	28.63/0.928	30.19/0.957	29.80/0.946	<u>31.28/0.965</u>	29.44/0.948	29.09/0.932	31.51/0.966

$1)m_3 + n_3) \prod_{i=1}^3 m_i)$ and $O(m_1 m_2 n_3 |D|)$, respectively. The computational complexity of SNN is $O(\sum_{i=1}^3 \min(m_1 m_2 m_3, \prod_{j \neq i} m_j^2))$. In summary, the forward computational complexity of the proposed method is $O(((K - 1)m_3 + n_3) \prod_{i=1}^3 m_i + m_1 m_2 n_3 |D| + \sum_{i=1}^3 \min(\prod_{j=1}^3 m_j, \prod_{j \neq i} m_j^2))$.

5. Experiments

To verify the performance of the proposed method, we conduct extensive experiments on simulated and real-world spatial-irregular multidimensional data. Since existing methods cannot be directly applied to spatial-irregular tensors, we consider existing methods with preprocessing for comparison. For traditional tensor factorization-based methods, we first pad the original spatial-irregular tensor with zeros into a regular tensor, and then apply tensor factorization-based methods to the resulting regular tensor. For matrix factorization-based methods, we first unfold the original spatial-irregular tensor as a matrix using *i*-fold operator, and then apply matrix factorization-based methods to the resulting unfolding matrix. The specific methods will be introduced in later different recovery tasks.

5.1. Experimental setting

Hyperparameters Settings: We give the detailed setting of key hyperparameters in our method for reproducibility. The maximum iteration number of the training iterations is set to 1000 and 200 for the simulated superpixel completion and denoising tasks, respectively, and 1000 for the HSI denoising and the spatial transcriptomics data completion tasks. The size of the intrinsic tensor \mathcal{Z} is set to $\lfloor \sqrt{a|D|} \rfloor \times \lfloor \sqrt{a|D|} \rfloor \times bn_3$, where the D is the index set of the irregular observation and n_3 are the length of the tubes of the irregular observation, and $\lfloor \cdot \rfloor$ denotes the rounding function. The scaling factor a is selected from the candidate set $\{0.05, 0.06, \dots, 0.09, 0.1\}$, while b is set to 4 for superpixel recovery experiments and 1 for HSI denoising and spatial transcriptomics data recovery experiments. And the number of the layers of the channel transform, i.e., K , is set to 2 for all the experiments. The trade-off parameters $\{\lambda_i\}_{i=1}^2$ are chosen from the candidate set $\{10^{-2}, 10^{-3}, 10^{-4}, 10^{-5}, 10^{-6}\}$.

Platform: All experiments are conducted on a server with an Intel Core i9-9900K 3.60-GHz CPU, 64 GB RAM, and an NVIDIA RTX 2080 Ti GPU.

5.2. Simulated experiments

To make a fair comparison, we adopt two simulated superpixel recovery experiments. Superpixels are generated by applying superpixel segmentation algorithms to images, presenting the non-rectangular spatial domain. Specifically, the simulated data is MSI superpixels extracted from the cave dataset¹ [45] using simple linear iterative clustering segmentation (SLIC) [20]. Performance is quantified by peak signal-to-

noise ratio (PSNR) and structural similarity (SSIM), where higher values indicate better recovery quality. We consider two tasks:

1) *Superpixel Denoising:* Two noise cases are considered. **Case 1** includes the Gaussian noise with a standard deviation 0.2 and **Case 2** includes the same Gaussian noise in **Case 1** and impulse noise with the ratio 0.05. Since adding noise requires regular inputs, we first pad the original irregular tensor with zeros into a regular tensor, then add noise according to the two cases, respectively. Finally, we extract the irregular portion as the observed irregular tensor. Comparisons include the low-rank matrix recovery (LRMR) [46], the total-variation-regularized low-rank matrix factorization (LRTV) [47], the total variation regularized low-rank tensor decomposition (LRTDTV) [48], the enhanced 3DTV regularization (E3DTV) [43], the hierarchical low-rank tensor factorization (HLRTF) [49], and the Learnable Representative Coefficient Image Denoiser (LRCID) [50]. We use the zero padding data as the observation for all compared methods in the denoising task since they are not suitable for irregular data.

2) *Superpixel Completion:* Sampling rates of 0.05, 0.1, and 0.15 are considered. Since sampling elements requires regular inputs, we first pad the original irregular tensor with zeros into a regular tensor, then randomly sample elements from the padded tensor with a given sampling rate. Finally, we extract the irregular portion as the observed irregular tensor. Compared methods include the low-rank tensor completion via smooth matrix factorization (SMF) [51], the tensor ring decomposition with rank minimization on latent space (TRLRF) [52], the framelet transformed TNN (FTNN) [33], the dictionary learning-based TNN (DTNN) [34], the fully connected tensor network decomposition (FCTN) [53], and the nonlinear transform induced TNN (NTTNN) [54]. For traditional tensor factorizations, the irregular tensor is recast as a regular tensor with tubes missing.

Tables 2 and **3** demonstrate the stable and superior performance of our proposed method on the denoising and completion for superpixels of MSI. The visualizations in **Figs. 8** and **9** show that IRTF generally preserves the structure of irregular data better compared with traditional tensor factorizations with zero padding. For example, the edges in the results of FTNN in **Fig. 9** and LRTDTV in **Fig. 8** exhibit noticeable color deviations compared to the ground truth images. These experimental results validate the effectiveness of our proposed method for superpixel denoising and completion.

5.3. Real data experiments

To examine the performance of our method on real-world spatial-irregular multidimensional data recovery and its benefits for downstream application, we conducted HSI denoising and transcriptomics data completion experiments and applied the recovered results to the downstream classification and clustering tasks.

5.3.1. Hyperspectral image denoising and classification

First, we consider the HSI classification task, which aims to assign land cover labels by categorizing pixels or segments based on spectral, textural, and contextual features. However, the complex appearance

¹ <https://www.cs.columbia.edu/CAVE/databases/multispectral/>

Table 3

The average numerical results of superpixel completion by different methods. The **best** and second-best values are highlighted.

Method	SMF	TRLRF	FTNN	DTNN	FCTN	NTTNN	IRTF	
Data	Sampling rate	PSNR(dB)/SSIM						
	0.05	26.84/0.936	26.28/0.879	23.38/0.889	26.52/0.912	26.03/0.881	<u>27.32/0.919</u>	<u>30.45/0.964</u>
	0.10	31.71/0.974	30.92/0.955	28.94/0.959	30.40/0.960	30.18/0.946	<u>31.87/0.970</u>	<u>34.01/0.981</u>
	0.15	34.79/0.987	33.28/0.973	31.83/0.977	33.45/0.979	33.25/0.969	<u>34.42/0.983</u>	<u>36.13/0.992</u>
	0.05	29.31/0.957	30.12/0.902	25.79/0.921	30.15/0.935	27.69/0.901	<u>33.49/0.966</u>	<u>37.27/0.987</u>
	0.10	36.26/0.984	33.15/0.947	30.96/0.967	34.21/0.975	34.25/0.969	<u>38.60/0.989</u>	<u>41.75/0.995</u>
	0.15	38.05/0.986	35.27/0.966	34.30/0.982	37.99/0.989	39.49/0.989	<u>41.47/0.994</u>	<u>44.18/0.997</u>
	0.05	28.71/0.944	26.96/0.885	26.72/0.921	26.65/0.882	27.01/0.900	<u>28.49/0.925</u>	<u>31.51/0.962</u>
	0.10	33.09/0.976	30.22/0.947	30.64/0.963	31.60/0.963	32.14/0.968	<u>32.62/0.974</u>	<u>36.02/0.987</u>
	0.15	34.84/0.983	32.70/0.971	32.96/0.976	35.37/0.985	34.77/0.982	<u>36.41/0.988</u>	<u>38.62/0.993</u>

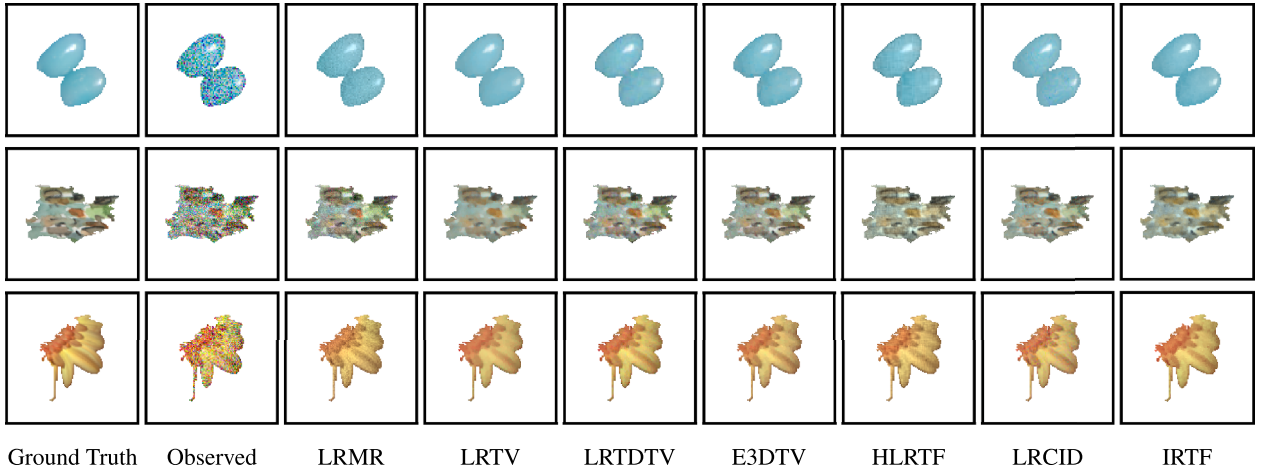


Fig. 8. Pseudo-color images of superpixel denoising results by compared methods, and our proposed IRTF, on simulated superpixel data *Jelly beans* with Case 1 (first row), *Watercolors* with Case 2 (second row), and *Flowers* with Case 2 (third row). (Note that the observation of all the compared methods is superpixels with zero padding).

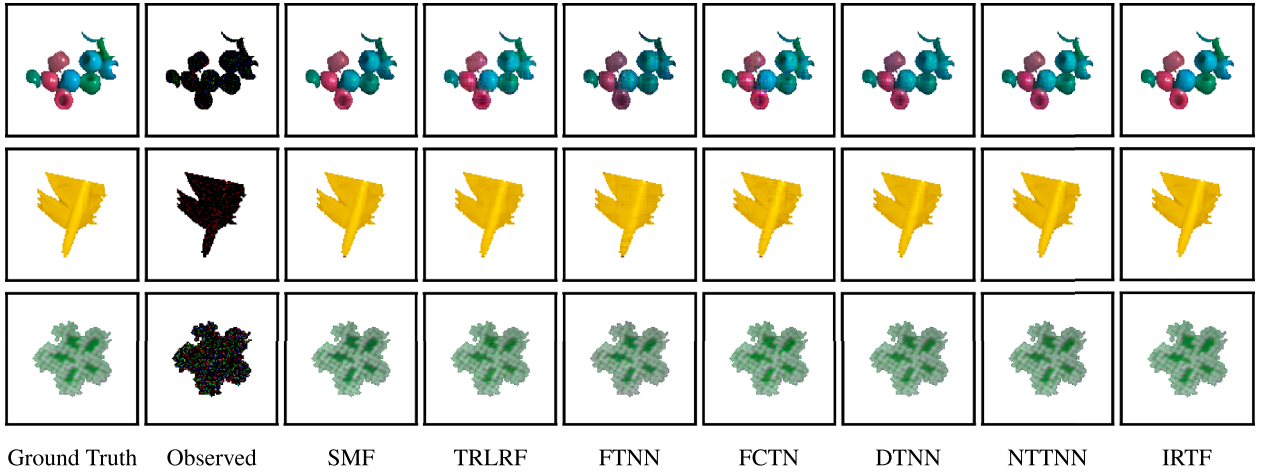


Fig. 9. Pseudo-color images of superpixel completion results by compared methods, and our proposed IRTF, on simulated superpixel data *Beads* with sampling rate 0.05 (first row), *Feathers* with sampling rate 0.1 (second row), and *Cloth* with sampling rate 0.15 (third row).

variations of geographic features pose a significant challenge. To address this, we propose a spatial-irregular tensor-based approach that utilizes spatial-irregular tensor representations for denoising and classification (as shown in Fig. 10). Unlike conventional denoising that overlooks region differences, our proposed method exploiting superpixel irregularity and semantics can thus boost classification performance.

Specifically, we use the noisy HSI *Indian Pines* dataset² (145 × 145 pixels, 224 bands, and 16 classes), which is segmented into superpixels using SLIC [20]. Our approach simultaneously denoises each superpixel while retaining structure. The reconstructed image

² https://www.ehu.eus/ccwintco/uploads/2/22/Indian_pines.mat

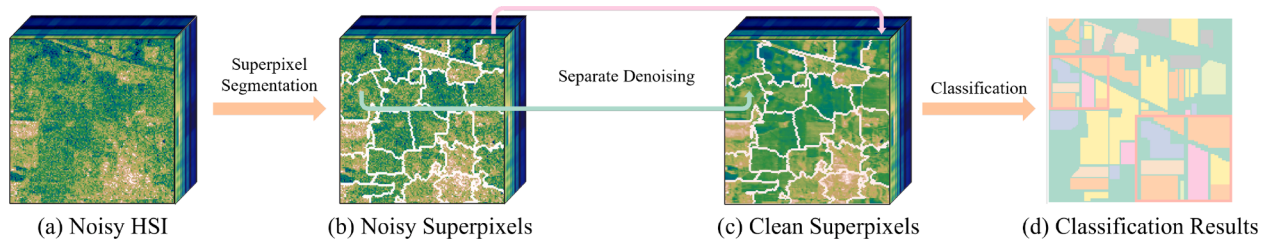


Fig. 10. The workflow of HSI classification using spatial-irregular tensor recovery on superpixels. The input noisy HSI (a) is first segmented into spatial-irregular superpixels (b). Then our proposed spatial-irregular tensor recovery method is applied to reduce noise within each superpixel separately. The denoised superpixels (c) are aggregated to reconstruct a cleaned HSI for subsequent land cover classification (d).

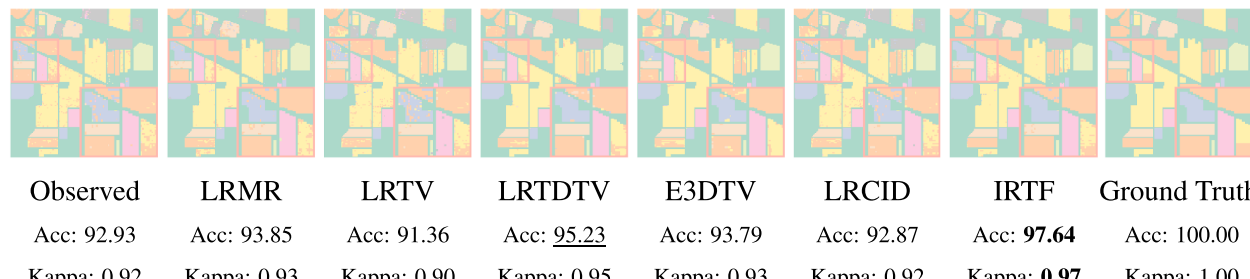


Fig. 11. Pseudo-color image, Acc (%), and Kappa of classification maps of the observation, completed images by different methods, and the ground-truth labels. The best and second-best values are highlighted.

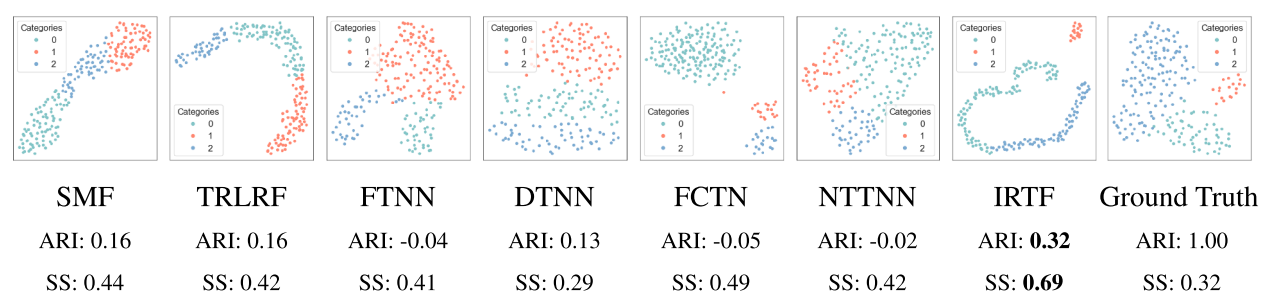


Fig. 12. Visual and numerical clustering results of spatial transcriptomics data of human heart data imputed by different methods. For visualization, UMAP [57] is used as the dimensionality reduction method.

is then classified using a baseline neural network³ (4 fully connected layers with dropout) [55]. Compared denoising methods are the same as those in the superpixel denoising experiment. All the denoising methods employ the same classifier, i.e., the fully connected neural network. Quantitative evaluation metrics include accuracy (Acc) and Cohen's kappa coefficient (Kappa).

Quantitative evaluation metrics and visualizations of the classification outcomes are provided in Fig. 11. The results suggest that our method enables more discriminative feature extraction versus the original noisy input or alternative denoising methods, leading to noticeable classification improvements. Our flexible framework leverages superpixel representations to handle noise in hyperspectral analysis to better preserve semantic information which is important for the downstream classification task.

5.3.2. Spatial transcriptomics data recovery and clustering

The spatial transcriptomic “method of the year 2020 by Nature Methods” is a high-throughput technique that captures gene expression data mapped to spatial coordinates in biological tissues. This generates spatial-irregular multidimensional data, with gene expression quanti-

fied across irregularly distributed spots on a tissue section. A salient characteristic of such data is its high proportion of zero entries, which includes the true negative entries and missing values (“dropout”). To demonstrate the utility of our proposed method, we applied it to recover the spatial transcriptomics data of human heart data [22] (see its visualization in Fig. 1 (b)).

Since no ground truth reference exists for this spatial transcription data, we considered the given expression values as the ground truth. We randomly sample 10% of the non-zero elements to generate the observed data. Then, we impute missing values by different methods and perform downstream clustering. Here, we employ the classical k-means [56] as the clustering method. Compared methods are the same as the superpixel completion experiment.

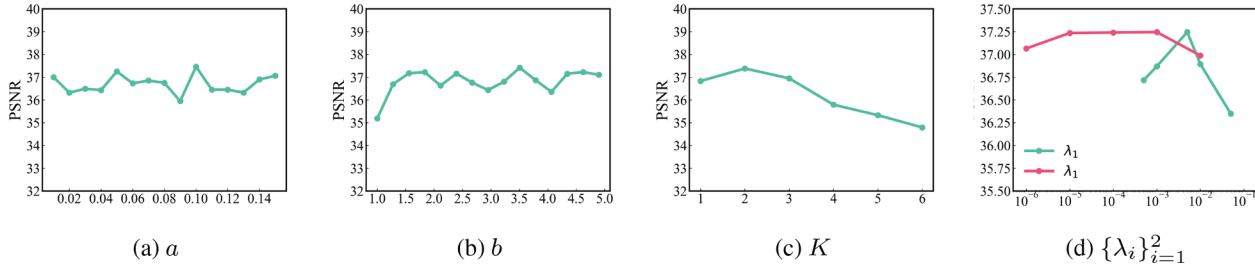
In Fig. 12, we provide both visual and numerical clustering results of spatial transcriptomics data of human heart data imputed by different methods. Here, we use adjusted rand index (ARI) [58] and silhouette score (SS) [59] as numerical metrics. We can observe that the clustering result of spatial transcriptomics data imputed by our method visually shows a better grouping of similar classes and better separation of different classes, meanwhile achieving the best ARI and SS values numerically compared to those obtained using competing methods. In summary, our method can benefit downstream applications as compared with competing methods.

³ <https://github.com/nshaud/DeepHyperX>

Table 4

The results of irregular superpixel denoising by IRTF with different items on *Egyptian Statue*. “–” shows that IRTF is incapable of spatial-irregular data without the spatial transform.

Channel Transform	Spatial Transform	Low-rankness Reg.	Local Smoothness Reg.	PSNR	SSIM
✗	✗	✗	✗	–	–
✗	✓	✗	✗	23.05	0.664
✓	✓	✗	✗	24.97	0.783
✓	✓	✗	✓	31.54	0.928
✓	✓	✓	✗	25.24	0.790
✓	✓	✓	✓	31.89	0.936

**Fig. 13.** The completion results by IRTF with different parameters.

5.4. Ablation study

In this section, we evaluate the impact of the crucial factors in our model for understanding their roles.

5.4.1. Roles of transforms and regularization

Our proposed IRTF-based recovery model consists of several important components: the **channel transform** for nonlinear structure exploration, the **spatial transform** for converting data to an irregular format. Additionally, the model incorporates regularizations, including TV-CST and SNN, to encourage **local smoothness** and **low-rankness**, respectively. To assess their impact, we conducted ablation experiments, and the results are presented in [Table 4](#). The results demonstrate that spatial transformation is key for handling spatial-irregular tensors in our proposed IRTF. Furthermore, it is evident that the meticulously designed components contribute to the superior performance of the proposed model.

5.4.2. Roles of hyperparameters

In our proposed model, several hyperparameters need to be adjusted during training. These include the scaling coefficients a and b that control the size of tensor \mathcal{Z} , the number of layers K for channel transform, and the trade-off parameters $\{\lambda_i\}_{i=1}^2$ for regularization terms TV-CST and SNN. We conduct ablation experiments to assess these hyperparameters' impact on our model's performance. The results shown in [Fig. 13](#) suggest that our model is robust to a , b , and λ_2 and that appropriate K and λ_1 can help our model achieve better results.

6. Conclusion

The emerging spatial-irregular data summons the development of a new tensor factorization for irregular tensors. In response, we meticulously designed the novel IRTF, which can fully capture the intrinsic spatial and channel information behind the spatial-irregular tensor. Additionally, the TV-CST regularization overcomes the limitations of traditional TV regularization for spatial-irregular tensors. Extensive experiments on real-world spatial-irregular tensors demonstrated the superior performance of the proposed IRTF and its significant advantages on downstream tasks. We believe our approach is a promising alternative for the emerging spatial-irregular data compared with existing methods.

CRediT authorship contribution statement

Jin-Yu Xie: Writing – original draft, Writing – review & editing, Methodology; **Hao Zhang:** Writing – review & editing, Conceptualization, Supervision; **Xi-Le Zhao:** Writing – review & editing, Supervision; **Yi-Si Luo:** Writing – review & editing.

Data availability

Data will be made available on request.

Declaration of competing interest

We have no relevant interests to disclose. We declare that we have no financial and personal relationships with other people or organizations that can inappropriately influence our work, there is no professional or other personal interest of any nature or kind in any product, service and/or company that could be construed as influencing the position presented in, or the review of, the manuscript entitled.

Acknowledgement

This research is supported by NSFC (No. 12371456, 12171072, 62131005, 12501649), Sichuan Science and Technology Program (No. 2024NSFJQ0038, 2021ZYD0007, 2024NSFSC0038), National Key Research and Development Program of China (No.2020YFA0714001).

Supplementary material

Supplementary material associated with this article can be found, in the online version, at [10.1016/j.knosys.2025.114372](https://doi.org/10.1016/j.knosys.2025.114372)

Appendix A. Proofs

A.1. Proof of [Theorem 1](#)

Proof. Suppose that $\mathcal{X} = h_{\mathbf{W}}(g_{\mathbf{H}}(\mathcal{Z}))$ and the spatial index set D is regular, where the ℓ_1 -norm of \mathcal{Z}, \mathbf{W} , and $\{\mathbf{H}_j\}_{j=1}^K$ is bounded by η . We use \mathcal{W} to denote $\text{ir-fold}(\mathbf{W}, D)$ for simplicity. Since $\tau(\cdot)$ is Lipschitz continuous with Lipschitz constant κ , we have that $\|\tau(\mathcal{A})\|_{\ell_1} \leq \kappa \|\mathcal{A}\|_{\ell_1}$ holds

for arbitrary \mathcal{A} . Then

$$\begin{aligned}
\|\mathbb{D}_x \mathcal{X}\|_{\ell_1} &= \|\mathcal{X}(2:n_1, :, :) - \mathcal{X}(1:n_1-1, :, :)\|_{\ell_1} \\
&= \|(g_{\mathbf{H}}(\mathcal{Z}) \times_D \mathbf{W})(2:n_1, :, :) - (g_{\mathbf{H}}(\mathcal{Z}) \times_D \mathbf{W})(1:n_1-1, :, :)\|_{\ell_1} \\
&= \|\mathcal{W}(2:n_1, :, :) \times_3 \text{unfold}_3(g_{\mathbf{H}}(\mathcal{Z})) \\
&\quad - \mathcal{W}(1:n_1-1, :, :) \times_3 \text{unfold}_3(g_{\mathbf{H}}(\mathcal{Z}))\|_{\ell_1} \\
&= \|(\mathbb{D}_x \mathcal{W}) \times_3 \text{unfold}_3(g_{\mathbf{H}}(\mathcal{Z}))\|_{\ell_1} \\
&\leq \|\mathbb{D}_x \mathcal{W}\|_{\ell_1} \|g_{\mathbf{H}}(\mathcal{Z})\|_{\ell_1} \\
&= \|\mathbb{D}_x \mathcal{W}\|_{\ell_1} \|\tau(\cdots \tau(\mathcal{Z} \times_3 \mathbf{H}_1) \times_3 \mathbf{H}_2 \cdots) \times_3 \mathbf{H}_K\|_{\ell_1} \\
&\leq \kappa^{K-1} \|\mathbb{D}_x \mathcal{W}\|_{\ell_1} \|\mathcal{Z}\|_{\ell_1} \prod_{i=1}^K \|\mathbf{H}_i\|_{\ell_1} \\
&\leq \kappa^{K-1} \eta^{K+1} \|\mathbb{D}_x \mathcal{W}\|_{\ell_1} \\
&= \kappa^{K-1} \eta^{K+1} \|\mathbb{D}_1 \mathbf{W}\|_{\ell_1}.
\end{aligned} \tag{A.1}$$

Similarly, we have $\|\mathbb{D}_y \mathcal{X}\|_{\ell_1} \leq \kappa^{K-1} \eta^{K+1} \|\mathbb{D}_2 \mathbf{W}\|_{\ell_1}$.

Next, we prove the third inequality. Since

$$\begin{aligned}
\|\mathbb{D}_z \mathcal{X}\|_{\ell_1} &= \|\mathcal{X}(:, :, 2:n_3) - \mathcal{X}(:, :, 1:n_3-1)\|_{\ell_1} \\
&= \|(g_{\mathbf{H}}(\mathcal{Z}) \times_D \mathbf{W})(:, :, 2:n_3) - (g_{\mathbf{H}}(\mathcal{Z}) \times_D \mathbf{W})(:, :, 1:n_3-1)\|_{\ell_1} \\
&= \|(\mathcal{W} \times_3 \text{unfold}_3(g_{\mathbf{H}}(\mathcal{Z}))) (2:n_3, :) \\
&\quad - (\mathcal{W} \times_3 \text{unfold}_3(g_{\mathbf{H}}(\mathcal{Z}))) (1:n_3-1, :)\|_{\ell_1} \\
&\leq \|\mathcal{W}\|_{\ell_1} \|\text{unfold}_3(g_{\mathbf{H}}(\mathcal{Z}))(2:n_3, :) \\
&\quad - \text{unfold}_3(g_{\mathbf{H}}(\mathcal{Z}))(1:n_3-1, :)\|_{\ell_1} \\
&\leq \eta \|\tau(\cdots \tau(\mathcal{Z} \times_3 \mathbf{H}_1) \times_3 \mathbf{H}_2 \cdots) \times_3 \mathbf{H}_K (:, :, 2:n_3) \\
&\quad - \tau(\cdots \tau(\mathcal{Z} \times_3 \mathbf{H}_1) \times_3 \mathbf{H}_2 \cdots) \times_3 \mathbf{H}_K (:, :, 1:n_3-1)\|_{\ell_1} \\
&\leq \eta \|\tau(\cdots \tau(\mathcal{Z} \times_3 \mathbf{H}_1) \times_3 \mathbf{H}_2 \cdots) \times_3 \mathbf{H}_{K-1}\|_{\ell_1} \|\mathbb{D}_3 \mathbf{H}_K\|_{\ell_1} \\
&\leq \eta \kappa^{K-1} \|\mathcal{Z}\|_{\ell_1} \prod_{i=1}^{K-1} \|\mathbf{H}_i\|_{\ell_1} \|\mathbb{D}_3 \mathbf{H}_K\|_{\ell_1} \\
&\leq \eta^{K+1} \kappa^{K-1} \|\mathbb{D}_3 \mathbf{H}_K\|_{\ell_1},
\end{aligned} \tag{A.2}$$

we have $\|\mathbb{D}_z \mathcal{X}\|_{\ell_1} \leq \eta^{K+1} \kappa^{K-1} \|\mathbb{D}_3 \mathbf{H}_K\|_{\ell_1}$. The proof is completed. \square

A.2. Proof of Theorem 2

Proof. To prove Theorem 2, we need the following inequality

$$\sum_{j=1}^{\min(r_1, r_2)} \sigma_j(\mathbf{T}_1 \mathbf{X} \mathbf{T}_2) \leq \sum_{j=1}^{\min(n, m)} \sigma_j(\mathbf{X}), \tag{A.3}$$

where $\mathbf{X} \in \mathbb{R}^{n \times m}$ is any matrix and $\mathbf{T}_1 \in \mathbb{R}^{r_1 \times n}$ and $\mathbf{T}_2 \in \mathbb{R}^{m \times r_2}$ are matrices which satisfy $\mathbf{T}_1 \mathbf{T}_1^\top = \mathbf{I}$ and $\mathbf{T}_2^\top \mathbf{T}_2 = \mathbf{I}$ [60]. In order to establish the Eq. 11, we will examine the cases where i is equal to 1, 2, and 3, respectively. We first prove the case that $i = 1$, then we have

$$\begin{aligned}
\sum_{j=1}^{q_1} \sigma_j(\text{unfold}_1(\mathcal{X})) &= \sum_{j=1}^{q_1} \sigma_j(\text{unfold}_1(h_{\mathbf{W}}(g_{\mathbf{H}}(\mathcal{Z})))) \\
&= \sum_{j=1}^{q_1} \sigma_j(\text{unfold}_1(\mathcal{Z} \times_3 \mathbf{H}_1 \times_D \mathbf{W})) \\
&= \sum_{j=1}^{q_1} \sigma_j(\text{unfold}_1(\mathcal{Z} \times_3 \mathbf{H}_1 \times_D (\mathbf{A} \otimes \mathbf{B})))
\end{aligned} \tag{A.4}$$

since $\text{vec}(\mathcal{Z}(:, :, 1))^\top (\mathbf{A} \otimes \mathbf{B}) = \text{vec}(\mathbf{B}^\top \mathcal{Z}(:, :, 1) \mathbf{A})^\top$, we have
 $\text{ir-unfold}(\mathcal{Z})(\mathbf{A} \otimes \mathbf{B}) = [\text{vec}(\mathbf{B}^\top \mathcal{Z}(:, :, 1) \mathbf{A})^\top; \text{vec}(\mathbf{B}^\top \mathcal{Z}(:, :, 2) \mathbf{A})^\top; \dots]$

$\text{vec}(\mathbf{B}^\top \mathcal{Z}(:, :, m_3) \mathbf{A})^\top]$, i.e., $\mathcal{Z} \times_D (\mathbf{A} \otimes \mathbf{B}) = \mathcal{Z} \times_2 \mathbf{A}^\top \times_1 \mathbf{B}^\top$. So we have

$$\begin{aligned}
\sum_{j=1}^{q_1} \sigma_j(\text{unfold}_1(\mathcal{X})) &= \sum_{j=1}^{q_1} \sigma_j(\text{unfold}_1(\mathcal{Z} \times_3 \mathbf{H}_1 \times_2 \mathbf{A}^\top \times_1 \mathbf{B}^\top)) \\
&= \sum_{j=1}^{q_1} \sigma_j(\mathbf{B}^\top \text{unfold}_1(\mathcal{Z} \times_3 \mathbf{H}_1 \times_2 \mathbf{A}^\top)) \\
&= \sum_{j=1}^{q_1} \sigma_j(\mathbf{B}^\top \text{unfold}_1(\mathcal{Z})(\mathbf{H}_1^\top \otimes \mathbf{A}))
\end{aligned} \tag{A.5}$$

since $(\mathbf{H}_1^\top \otimes \mathbf{A})^\top (\mathbf{H}_1^\top \otimes \mathbf{A}) = (\mathbf{H}_1 \otimes \mathbf{A}^\top)(\mathbf{H}_1^\top \otimes \mathbf{A}) = (\mathbf{H}_1 \mathbf{H}_1^\top \otimes \mathbf{A}^\top \mathbf{A}) = (\mathbf{I} \otimes \mathbf{I}) = \mathbf{I}$. So we have

$$\begin{aligned}
\sum_{j=1}^{q_1} \sigma_j(\text{unfold}_1(\mathcal{X})) &= \sum_{j=1}^{q_1} \sigma_j(\mathbf{A}^\top \text{unfold}_1(\mathcal{Z})(\mathbf{H}_1^\top \otimes \mathbf{B})) \\
&\leq \sum_{j=1}^{p_1} \sigma_j(\text{unfold}_1(\mathcal{Z})),
\end{aligned} \tag{A.6}$$

where $q_1 = \min(n_1, n_2 n_3)$ and $p_1 = \min(m_1, m_2 m_3)$. Next, We prove the case that $i = 2$, then we have

$$\begin{aligned}
\sum_{j=1}^{q_2} \sigma_j(\text{unfold}_2(\mathcal{X})) &= \sum_{j=1}^{q_2} \sigma_j(\text{unfold}_2(\mathcal{Z} \times_3 \mathbf{H}_1 \times_D \mathbf{W})) \\
&= \sum_{j=1}^{q_2} \sigma_j(\text{unfold}_2(\mathcal{Z} \times_3 \mathbf{H}_1 \times_D (\mathbf{A} \otimes \mathbf{B}))) \\
&= \sum_{j=1}^{q_2} \sigma_j(\text{unfold}_2(\mathcal{Z} \times_3 \mathbf{H}_1 \times_2 \mathbf{A}^\top \times_1 \mathbf{B}^\top)) \\
&= \sum_{j=1}^{q_2} \sigma_j(\mathbf{A}^\top \text{unfold}_2(\mathcal{Z})(\mathbf{H}_1^\top \otimes \mathbf{B})) \\
&\leq \sum_{j=1}^{p_2} \sigma_j(\text{unfold}_2(\mathcal{Z})),
\end{aligned} \tag{A.7}$$

where $q_2 = \min(n_2, n_1 n_3)$ and $p_2 = \min(m_2, m_1 m_3)$. Last, We prove the case that $i = 3$, then we have

$$\begin{aligned}
\sum_{j=1}^{q_3} \sigma_j(\text{unfold}_3(\mathcal{X})) &= \sum_{j=1}^{q_3} \sigma_j(\text{unfold}_3(\mathcal{Z} \times_3 \mathbf{H}_1 \times_D \mathbf{W})) \\
&= \sum_{j=1}^{q_3} \sigma_j(\mathbf{H}_1 \text{unfold}_3(\mathcal{Z}) \mathbf{W}) \\
&\leq \sum_{j=1}^{p_3} \sigma_j(\text{unfold}_3(\mathcal{Z})),
\end{aligned} \tag{A.8}$$

where $q_3 = \min(n_3, n_1 n_2)$ and $p_3 = \min(m_3, m_1 m_2)$. Thus, the inequality holds:

$$\begin{aligned}
S(\mathcal{Z}) &= \sum_{i=1}^3 \sum_j \sigma_j(\text{unfold}_i(\mathcal{Z})) \\
&\geq \sum_{i=1}^3 \sum_j \sigma_j(\text{unfold}_i(\mathcal{X})) \\
&= S(\mathcal{X}).
\end{aligned} \tag{A.9}$$

\square

Appendix B. More Experiment Results

B.1. More results of superpixel recovery

Furthermore, we have provided additional visual results of superpixel recovery in Figs. B.1–B.5. Our proposed model demonstrates superior effectiveness and stability compared to existing methods in the context of superpixel recovery.

B.2. More results of hyperspectral image recovery and classification

We first evaluate the impact of the number of segmented superpixels on the image denoising performance. As the number of pixels within each superpixel varies, the amount of semantic information contained within them evidently changes, directly affecting the effectiveness of the IRTF for irregular data restoration. Consequently, we conducted relevant experiments to assess this impact. Specifically, in the context of HSI denoising tasks, we use the HSI *Pavia University* dataset,⁴ consider the Gaussian noise with standard deviation 0.1, and control the superpixel segmentation algorithm to obtain different quantities of superpixels, followed by applying our IRTF to restore all superpixels within the HSI. The experimental outcomes are displayed in the Fig. B.6.

References

- [1] Y. Zhang, Z. Tu, J. Lu, C. Xu, L. Shen, Fusion of low-rankness and smoothness under learnable nonlinear transformation for tensor completion, *Knowl. Based Syst.* 296 (2024) 111917.
- [2] Z.-Y. Chen, X.-L. Zhao, J. Lin, Y. Chen, Nonlocal-based tensor-average-rank minimization and tensor transform-sparsity for 3D image denoising, *Knowl. Based Syst.* 244 (2022) 108590.
- [3] X. Zheng, Y. Yuan, X. Lu, A target detection method for hyperspectral image based on mixture noise model, *Neurocomputing* 216 (2016) 331–341.
- [4] Z. Liang, K. Zhao, G. Liang, S. Li, Y. Wu, Y. Zhou, MAXFormer: enhanced transformer for medical image segmentation with multi-attention and multi-scale features fusion, *Knowl. Based Syst.* 280 (2023) 110987.
- [5] B. Barman, S. Patra, Variable precision rough set based unsupervised band selection technique for hyperspectral image classification, *Knowl. Based Syst.* 193 (2020) 105414.
- [6] G. Zhao, B. Tu, H. Fei, N. Li, X. Yang, Spatial-spectral classification of hyperspectral image via group tensor decomposition, *Neurocomputing* 316 (2018) 68–77.
- [7] Q. Song, H. Ge, J. Caverlee, X. Hu, Tensor completion algorithms in big data analytics, *ACM Trans. Knowl. Discov. Data* 13 (1) (2019), 1–48, 6.
- [8] D.M. Dunlavy, T.G. Kolda, E. Acar, Temporal link prediction using matrix and tensor factorizations, *ACM Trans. Knowl. Discov. Data* 5 (2) (2011), 1–27, 10.
- [9] F.L. Hitchcock, The expression of a tensor or a polyadic as a sum of products, *J. Math. Phys.* 6 (1–4) (1927) 164–189.
- [10] G.J.H.deM. Goullart, G. Favier, An algebraic solution for the candecomp/PARAFAC decomposition with circulant factors, *SIAM J. Matrix Anal. Appl.* 35 (4) (2014) 1543–1562.
- [11] L.R. Tucker, Some mathematical notes on three-mode factor analysis, *Psychometrika* 31 (3) (1966) 279–311.
- [12] P. Shao, D. Zhang, G. Yang, J. Tao, F. Che, T. Liu, Tucker decomposition-based temporal knowledge graph completion, *Knowl. Based Syst.* 238 (2022) 107841.
- [13] C. Lu, J. Feng, Y. Chen, W. Liu, Z. Lin, S. Yan, Tensor robust principal component analysis with a new tensor nuclear norm, *IEEE Trans. Pattern Anal. Mach. Intell.* 42 (4) (2020) 925–938.
- [14] L. Chen, X. Jiang, X. Liu, Z. Zhou, Robust low-rank tensor recovery via nonconvex singular value minimization, *IEEE Trans. Image Process.* 29 (2020) 9044–9059.
- [15] J.-Y. Li, J.-Y. Xie, Y.-S. Luo, X.-L. Zhao, J.-L. Wang, H2TF for hyperspectral image denoising: where hierarchical nonlinear transform meets hierarchical matrix factorization, *IEEE Geosci. Remote Sens. Lett.* 20 (2023), 1–5, 5506705.
- [16] A. Cichocki, N. Lee, I. Oseledets, A.-H. Phan, Q. Zhao, D.P. Mandic, Tensor Networks for Dimensionality Reduction and Large-scale Optimization: Part 2 Applications and Future Perspectives, *Tensor networks for dimensionality reduction and large-scale optimization: part 2 applications and future perspectives, Now Foundations and Trends*, 2017.
- [17] I.V. Oseledets, Tensor-train decomposition, *SIAM J. Sci. Comput.* 33 (5) (2011) 2295–2317.
- [18] Q. Zhao, G. Zhou, S. Xie, L. Zhang, A. Cichocki, Tensor Ring Decomposition, 2016. arXiv:1606.05535
- [19] A. Kirillov, E. Mintun, N. Ravi, H. Mao, C. Rolland, L. Gustafson, T. Xiao, S. Whitehead, A.C. Berg, W.-Y. Lo, P. Dollár, R. Girshick, Segment Anything, 2023. arXiv:2304.02643
- [20] R. Achanta, A. Shaji, K. Smith, A. Lucchi, P. Fua, S. Süstrunk, SLIC Superpixels compared to state-of-the-art superpixel methods, *IEEE Trans. Pattern Anal. Mach. Intell.* 34 (11) (2012) 2274–2282.
- [21] Z. Li, J. Chen, Superpixel Segmentation Using Linear Spectral Clustering, in: *Proc. IEEE Conf. Comput. Vis. Pattern Recognit.*, 2015, pp. 1356–1363.
- [22] M. Asp, S. Giacomello, L. Larsson, C. Wu, D. Fürth, X. Qian, E. Wärdell, J. Custodio, J. Reimegård, F. Salmen, et al., A spatiotemporal organ-wide gene expression and cell atlas of the developing human heart, *Cell* 179 (7) (2019) 1647–1660.e19.
- [23] Q. Zhao, L. Zhang, A. Cichocki, Bayesian CP factorization of incomplete tensors with automatic rank determination, *IEEE Trans. Pattern Anal. Mach. Intell.* 37 (9) (2015) 1751–1763.
- [24] J. Liu, P. Musialski, P. Wonka, J. Ye, Tensor completion for estimating missing values in visual data, *IEEE Trans. Pattern Anal. Mach. Intell.* 35 (1) (2013) 208–220.
- [25] Y. Xu, R. Hao, W. Yin, Z. Su, Parallel matrix factorization for low-rank tensor completion, *Inverse Probl. Imaging* 9 (2) (2015) 601–624.
- [26] P.-L. Wu, X.-L. Zhao, M. Ding, Y.-B. Zheng, L.-B. Cui, T.-Z. Huang, Tensor ring decomposition-based model with interpretable gradient factors regularization for tensor completion, *Knowl. Based Syst.* 259 (2023) 110094.
- [27] T.-H. Zhang, J.-L. Zhao, S. Fang, Z. Li, M.-G. Gong, Full-mode-augmentation tensor-train rank minimization for hyperspectral image inpainting, *IEEE Trans. Geosci. Remote Sensing* 62 (2024), 1–13, 5500913.
- [28] J.A. Bengua, H.N. Phien, H.D. Tuan, M.N. Do, Efficient tensor completion for color image and video recovery: low-rank tensor train, *IEEE Trans. Image Process.* 26 (5) (2017) 2466–2479.
- [29] H. Zhang, X.-L. Zhao, T.-X. Jiang, M.K. Ng, T.Z. Huang, Multiscale feature tensor train rank minimization for multidimensional image recovery, *IEEE Trans. Cybern.* 52 (2022) 13395–13410.
- [30] M.E. Kilmer, C.D. Martin, Factorization strategies for third-order tensors, *Linear Alg. Appl.* 435 (2011) 641–658.
- [31] Z. Zhang, G. Ely, S. Aeron, N. Hao, M. Kilmer, Novel methods for multilinear data completion and de-noising based on tensor-SVD, in: *Proc. IEEE Conf. Comput. Vis. Pattern Recognit.*, 2014, pp. 3842–3849.
- [32] C. Lu, X. Peng, Y. Wei, Low-rank tensor completion with a new tensor nuclear norm induced by invertible linear transforms, in: *Proc. IEEE Conf. Comput. Vis. Pattern Recognit.*, 2019, p. 5996–6004.
- [33] T.-X. Jiang, M.K. Ng, X.-L. Zhao, T.-Z. Huang, Framelet representation of tensor nuclear norm for third-order tensor completion, *IEEE Trans. Image Process.* 29 (2020) 7233–7244.
- [34] T.-X. Jiang, X.-L. Zhao, H. Zhang, M.K. Ng, Dictionary learning with low-rank coding coefficients for tensor completion, *IEEE Trans. Neural Netw. Learn. Syst.* 34 (2) (2021) 932–946.
- [35] T.G. Kolda, B.W. Bader, Tensor decompositions and applications, *SIAM Rev.* 51 (3) (2009) 455–500.
- [36] I. Perros, E.E. Papalexakis, F. Wang, R. Vuduc, E. Searles, M. Thompson, J. Sun, SPARTAN: scalable PARAFAC2 for large & sparse data, in: *Proc. ACM SIGKDD Int. Conf. Knowl. Discov. Data Min.*, 2017, p. 375–384.
- [37] K. Yin, A. Afshar, J.C. Ho, W.K. Cheung, C. Zhang, J. Sun, LogPar: logistic PARAFAC2 factorization for temporal binary data with missing values, in: *Proc. ACM SIGKDD Int. Conf. Knowl. Discov. Data Min.*, 2020, p. 1625–1635.
- [38] J.-G. Jang, J. Lee, J. Park, U. Kang, Accurate PARAFAC2 decomposition for temporal irregular tensors with missing values, in: *Proc. IEEE Int. Conf. Big Data*, 2022, pp. 982–991.
- [39] T. Kwon, J. Ko, J. Jung, J.-G. Jang, K. Shin, Compact decomposition of irregular tensors for data compression: from sparse to dense to high-order tensors, in: *Proc. ACM SIGKDD Int. Conf. Knowl. Discov. Data Min.*, 2024, p. 1451–1462.
- [40] A. Afshar, I. Perros, E.E. Papalexakis, E. Searles, J. Ho, J. Sun, COPA: constrained PARAFAC2 for sparse and large datasets, in: *Proc. ACM Int. Conf. Inf. Knowl. Manag.*, 2018, p. 793–802.
- [41] Y. Ren, J. Lou, L. Xiong, J.C. Ho, Robust irregular tensor factorization and completion for temporal health data analysis, in: *Proc. ACM Int. Conf. Inf. Knowl. Manag.*, 2020, p. 1295–1304.
- [42] J.-G. Jang, U. Kang, DPar2: fast and scalable PARAFAC2 decomposition for irregular dense tensors, in: *Proc. IEEE Int. Conf. Data Eng.*, 2022, pp. 2454–2467.
- [43] J. Peng, Q. Xie, Q. Zhao, Y. Wang, L. Yee, D. Meng, Enhanced 3DTV regularization and its applications on HSI denoising and compressed sensing, *IEEE Trans. Image Process.* 29 (2020) 7889–7903.
- [44] D.P. Kingma, J. Ba, Adam: a method for stochastic optimization, in: *Proc. Int. Conf. Learn. Represent.*, 2015.
- [45] F. Yasuma, T. Mitsunaga, D. Iso, S.K. Nayar, Generalized assorted pixel camera: postcapture control of resolution, dynamic range, and spectrum, *IEEE Trans. Image Process.* 19 (9) (2010) 2241–2253.
- [46] H. Zhang, W. He, L. Zhang, H. Shen, Q. Yuan, Hyperspectral image restoration using low-rank matrix recovery, *IEEE Trans. Geosci. Remote Sensing* 52 (8) (2014) 4729–4743.
- [47] W. He, H. Zhang, L. Zhang, H. Shen, Total-variation-regularized low-rank matrix factorization for hyperspectral image restoration, *IEEE Trans. Geosci. Remote Sensing* 54 (1) (2016) 178–188.
- [48] Y. Wang, J. Peng, Q. Zhao, Y. Leung, X.-L. Zhao, D. Meng, Hyperspectral image restoration via total variation regularized low-rank tensor decomposition, *IEEE J. Sel. Top. Appl. Earth Observ. Remote Sens.* 11 (4) (2018) 1227–1243.

⁴ <https://www.ehu.eus/ccwintco/uploads/e/e3/Pavia.mat>

- [49] Y. Luo, X. Zhao, D. Meng, T. Jiang, HLRTF: hierarchical low-rank tensor factorization for inverse problems in multi-dimensional imaging, in: Proc. IEEE Conf. Comput. Vis. Pattern Recognit., 2022, pp. 19281–19290.
- [50] J. Peng, H. Wang, X. Cao, Q. Zhao, J. Yao, H. Zhang, D. Meng, Learnable representational coefficient image denoiser for hyperspectral image, *IEEE Trans. Geosci. Remote Sensing* 62 (2024), 1–16, 5506516.
- [51] Y.-B. Zheng, T.-Z. Huang, T.-Y. Ji, X.-L. Zhao, T.-X. Jiang, T.-H. Ma, Low-rank tensor completion via smooth matrix factorization, *Appl. Math. Model.* 70 (2019) 677–695.
- [52] L. Yuan, C. Li, D. Mandic, J. Cao, Q. Zhao, Tensor ring decomposition with rank minimization on latent space: an efficient approach for tensor completion, in: Proc. AAAI Conf. Artif. Intell., 2019.
- [53] Y.-B. Zheng, T.-Z. Huang, X.-L. Zhao, Q. Zhao, T.-X. Jiang, Fully-connected tensor network decomposition and its application to higher-order tensor completion, in: Proc. AAAI Conf. Artif. Intell., 35, 2021, pp. 11071–11078.
- [54] B.-Z. Li, X.-L. Zhao, T.-Y. Ji, X.-J. Zhang, T.-Z. Huang, Nonlinear transform induced tensor nuclear norm for tensor completion, *J. Sci. Comput.* 92 (3) (2022).
- [55] N. Audebert, B. Le Saux, S. Lefevre, Deep learning for classification of hyperspectral data: a comparative review, *IEEE Geosci. Remote Sens. Mag.* 7 (2) (2019) 159–173, 1–16, 5506516.
- [56] J. MacQueen, et al., Some methods for classification and analysis of multivariate observations, in: Proc. Berkeley Symp. Math. Stat. Prob., 1, 1967, pp. 281–297.
- [57] L. McInnes, J. Healy, N. Saul, L. Großberger, UMAP: uniform manifold approximation and projection, *J. of Open Source Softw.* 3 (29) (2018) 861.
- [58] L. Hubert, P. Arabie, Comparing partitions, *J. Classif.* 2 (1) (1985) 193–218.
- [59] P.J. Rousseeuw, Silhouettes: a graphical aid to the interpretation and validation of cluster analysis, *J. Comput. Appl. Math.* 20 (1987) 53–65.
- [60] S. Liu, J. Leng, X.-L. Zhao, H. Zeng, Y. Wang, J.-H. Yang, Learnable spatial-spectral transform-based tensor nuclear norm for multi-dimensional visual data recovery, *IEEE Trans. Circuits. Syst. Video Technol.* (2023), 3633–3646.